Anion-oriented solvation regulation of a dual-salt electrolyte for lithium metal batteries

Yaqi Zhang [a,1], Pengbin Lai [a,1], Xiaodie Deng [a], Peng Zhang [b,*], Jinbao Zhao [a,b,*]

[a] State-Province Joint Engineering Laboratory of Power Source Technology for New Energy Vehicle, Engineering Research Center of Electrochemical Technology, Ministry of Education, College of Chemistry and Chemical Engineering, Xiamen University, Xiamen 361005 PR China
[b] College of Energy, Xiamen University, Xiamen 361102 PR China

ARTICLE INFO

ABSTRACT

Designing suitable electrolytes and interphases is crucial for lithium metal batteries (LMBs), which are susceptible to excessive side reactions and lithium dendrite at the anode. Regulating the solvation ability of solvents and anions to tune the solvation structure and constructing an appropriate solid electrolyte interphase (SEI) are effective strategies for these problems. Herein, two different dissociated lithium salts (LiTFSI and LiBF$_4$) are screened to study the anion-oriented solvation regulation for SEI formation at the anode. It is found that BF$_4^-$ is less likely to be displaced from the inner layer by solvents compared to TFSI$^-$. Moreover, the resulting SEI with either an overly high or low content of inorganic components is not advantageous for long-term cycling performance. On the contrary, the dual salt electrolyte not only preferentially decomposes to form protective and balanced SEI with low impedance, but also maintains favorable bulk ion transport down to -40 °C. As a result, 4.3 V Li||LiCoO$_2$ full cells using the dual salt electrolyte deliver 88.7 % capacity retention after 200 cycles at 1C. This work highlights the significance of anion-oriented regulation in optimizing the performance of LMBs.

1. Introduction

Lithium metal anodes (LMAs) have been widely studied due to their high energy density (3860 mAh/g) and low reduction potential (-3.04 V vs. standard hydrogen electrode). However, compared to the intercalation and deintercalation of Li$^+$ in graphite during charge/discharge processes, the continuous plating and stripping of Li$^+$ can expose more fresh Li metal reacting with electrolyte [1–4]. Ongoing consumption and regeneration of the solid electrolyte interphase (SEI) with the uncontrollable growth of Li dendrites severely limit the practical application of LMA. The SEI formed in situ originates from the decomposition of electrolyte components, making the rational design of electrolytes to optimize SEI quality crucial [5,6].

Recent research has increasingly highlighted the key role of solvation structure in explaining the implicit relationship with the different performances of batteries. The solvation structure, formed by ions, solvents and their complex electrostatic interaction, can be divided into solvent-separated ion pair (SSIP), contact ion pair (CIP, an anion coordinating to one Li$^+$ cation) and aggregate (AGG, two or more anions coordinating to one Li$^+$ cation) [7]. In conventional 1 M electrolytes, the solvation structure centered around Li$^+$ is primarily solvent-dominated with a high proportion of SSIP. However, in high-concentration electrolytes [8,9] (HCEs), localized high-concentration electrolytes [10–12] (LHCEs) and weakly solvating electrolytes [13,14] (WSEs), the ratio of SSIP decreases significantly. Consequently, the lowest unoccupied molecular orbital (LUMO) shifts from the solvent to the anion, leading to greater anion incorporation into the SEI with an increased content of inorganic components [15,16]. It is generally considered that the inorganic components of the SEI, such as LiF and Li$_2$O, exhibit higher ionic conductivity and mechanical strength compared to organic components [17–20]. Therefore, designing an appropriate SEI based on the competitive coordination of solvents and anions with Li$^+$ is feasible. In other words, it is worthwhile to clarify the strong correlation between the solvating power of solvents and anions and the solvation structure as well as the quality of SEI.

Compared to the extensive research on solvents molecular design, including adjustments to chain length, variations in the types and positions of functional groups, and the introduction of high steric hindrance groups, the variety of anions has received relatively little exploration and investigation [21–23]. Among them, lithium bis

* Corresponding authors.
  E-mail addresses: pengzhang@xmu.edu.cn (P. Zhang), jbzhao@xmu.edu.cn (J. Zhao).
  [1] These authors contributed equally to this work.

(fluorosulfonyl)imide (LiFSI) and lithium bis(trifluoromethylsulphonyl) imide (LiTFSI), as highly dissociated salts, are often selected as the main salts of HCEs and LHCEs to ensure sufficient solubility, while there is relatively little discussion on other salts. Therefore, it is worth exploring how anions with different coordination degrees affect the solvation structure and electrochemical performance.

In this work, we systematically studied different solvation structure and interfacial chemistry for electrolytes with different anion coordination scenarios. Primarily, ethylene glycol diethyl ether (DEE) and fluoroethylene carbonate (FEC) known for good compatibility with LMA are used as the solvents. The intrinsic properties of the anions, such as size and binding energy, are leveraged to screen appropriate lithium salts with different dissociation (Fig. 1a). LiBF$_4$ possesses a smaller ionic radius and stronger binding ability, whereas LiTFSI exhibits the opposite characteristics [24]. Moreover, the differences in volume and binding energy between them are the most pronounced. Therefore, investigating the solvation structure in the presence of these two representative and significantly different salt anions will help distinguish their respective roles in the formation of the interphase components. Although lithium difluorophosphate (LiDFP) has a relatively negative binding energy, its poor solubility excludes it from consideration (Fig. S1). Additionally, we hope that the LUMO energy levels of the salts are as similar as possible. Notably, although LiClO$_4$ also satisfies the above two requirements, the reduction stability of LiClO$_4$ is significantly poorer than that of LiTFSI. Namely, if LiClO$_4$ is employed instead of LiBF$_4$, even with a small proportion of anion-cation pairs (AGG or CIP), it may lead to the preferential decomposition of the salt. Under such circumstances, the correlation between the anion coordination situation and the decomposition process is hard to discern, so LiClO$_4$ is excluded from study. Therefore, it is representative that LiTFSI and LiBF$_4$ are selected as the research objects. To accentuate anion coordination differences while ensuring adequate solubility, a moderate concentration of 2 M is chosen. It is found that TFSI$^-$ is less likely to enter the inner Li$^+$ solvation sheath, and the resulting solvent-derived SEI fails to effectively protect the LMA. In contrast, the presence of BF$_4^-$ can significantly increase the proportion of CIP and AGG, promoting the preferential decomposition of anions. However, the aggregation of small-sized BF$_4^-$ around Li$^+$ also increases the extent of anion decomposition. As a result, the SEI formed in electrolytes containing only BF$_4^-$ salt exhibits a higher inorganic content and greater thickness, which in turn increases the interfacial resistance. Particularly, the dual-salt electrolyte achieves a protective SEI with moderate inorganic content and good bulk ion transfer, resulting in excellent compatibility with LMA and outstanding cycling performance (Fig. 1b).

2. Experimental Section

2.1. Electrolyte Preparation

Ethylene glycol diethyl ether (DEE, 99 %) was purchased from Aladdin. Lithium bis(trifluoromethylsulphonyl)imide (LiTFSI, 99 %), lithium tetrafluoroborate (LiBF$_4$, 99.5 %) and fluoroethylene carbonate (FEC, 99 %) were provided by Zhangjiagang Guotai Huarong New Chemical Materials Co., Ltd. All the electrolytes were prepared and stored in an argon-filled glovebox with O$_2$ and H$_2$O level under 0.5 ppm. A homogeneous mixed solvent, DF73, was prepared by mixing DEE and FEC in a 7:3 vol ratio. LiTFSI or LiBF$_4$ was then dissolved in DF73 to form 2 mol/L electrolytes, denoted as 2 T and 2B, respectively. And 1 mol/L LiTFSI or 1 mol/L LiBF$_4$ in DF73 was marked as 1 T or 1B. The TB electrolyte was prepared similarly, with 1 mol/L LiTFSI and 1 mol/L LiBF$_4$ in DF73.

2.2. Material characterizations

Nuclear Magnetic Resonance (NMR) of ^{7}Li, ^{17}O, ^{19}F were tested by AVANCE NEO 500 MHz digital FT-NMR spectrometer. The solution of 0.1 M LiClO$_4$ in D$_2$O was encapsulated inside the capillary to serve as the internal standard in the NMR test, preventing its direct contact with the electrolyte. Raman spectra ere measured by HORIBA FRANCE using the laser of 532 nm. Fourier-transform infrared spectra (FTIR) were measured using a Nicolet iS50 spectrometer in absorption mode. The SEM (scanning electron microscope) images of deposited lithium on copper, cycled lithium metal anodes and LCO cathodes were obtained by Hitachi S-4800. The chemical composition of SEI on anodes or CEI on cathodes were analyzed by X-ray photoelectron spectroscopy (XPS, Thermo Scientific ESCALAB Xi +). For SEM and XPS tests, the cycled LCO electrodes and lithium metal anodes were rinsed with DEE solvent for three times in a glove box. During transportation process, these samples were stored in well-sealed containers to avoid direct contact with air.

2.3. Electrochemical Measurements

The active materials (LCO or NCM523), conducting agent (acetylene black) and binder (polyvinylidene fluoride) were mixed at a weight ratio of 8:1:1 or 94.5:2.5:3 with adequate 1-methyl-2-pyrrolidinone (NMP) to obtain the uniform slurry. Then the slurry was cast on aluminum foil and dried in 80 °C vacuum oven overnight. The sheet was punched into discs of 12 mm diameter with mass loading of 4–5 mg cm^{-2} or 12–13 mg cm^{-2}. Cell assembly was carried out in an Ar-filled glovebox with O$_2$ and
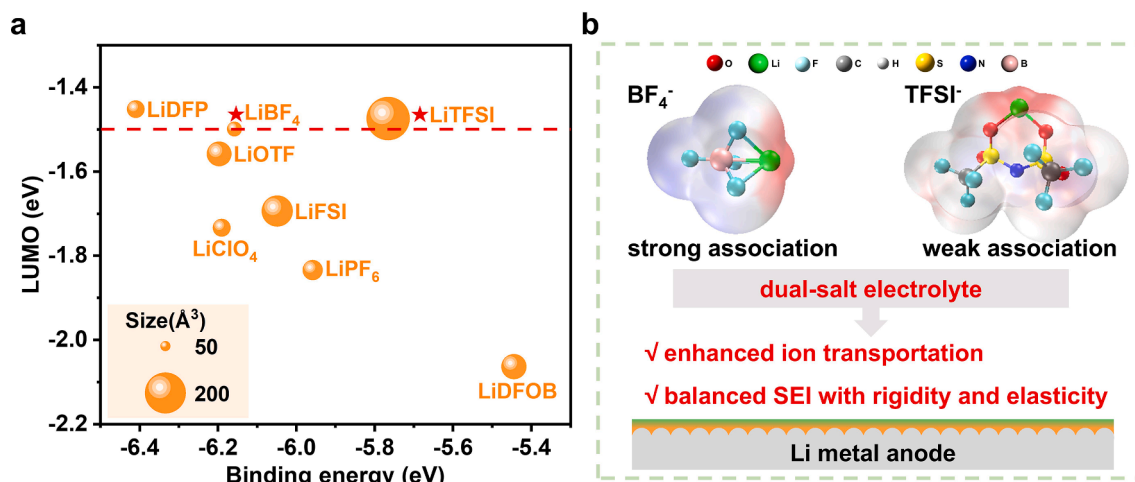

Fig. 1. (a) The selection of lithium salts based on the binding energy of anion with Li$^+$ (x-axis), the calculated LUMO of salt (y-axis), and volume of anion (scatter size). (b) Scheme of design principle for the dual-salt electrolyte used with lithium metal anode.

H$_2$O level under 0.5 ppm. CR2016 coins were assembled using the as-prepared discs as cathode, the Li metal foils with the thickness of 1000 μm or 50 μm and diameter of 12 mm as anode, and Celgard 2500 as separator. The ionic conductivities of the electrolytes were obtained using Pt||Pt electrode (Leici, China) and the viscosity was measured with the VM-10A-L viscometer. Different temperature environments were provided by DC-8006 incubator and cells for − 40 ℃ cycling test were placed in Meiling Biology & Medical DW-HW50 ultra-low freezer. The rate and cycling tests were conducted on a Neware test system. For measuring the CE of Li, fabricated Li||Cu cells were first discharged at the current density of 0.5 mA cm^{-2} for 10 h and charged to 1 V. Then, after 10 cycles of discharging and charging for 2 h each time at the same current, the cells were charged to 1 V for the last time to strip all the lithium [25]. The Li||LCO or Li||NCM523 cells were rested for 8 h after fabrication and activated 2 cycles at 0.1C (1C = 160 mA g^{-1} for LCO and 170 mA g^{-1} for NCM523), then cycled at 1C. For the low-temperature discharge tests, the charging process of the cells was carried out at room temperature, and then the cells were discharged at specific temperatures. Regarding the low-temperature cycling tests, the cells were activated for one cycle at room temperature before cycling at a specific temperature and rate. Li$^+$ transference number was calculated according to the following equation:

$$t_{Li^+} = \frac{I_s(\Delta V - I_0 R_0)}{I_0(\Delta V - I_s R_s)}$$

I_0 and I_s are the currents of initial and stable states, R_0 and R_s are the resistances of initial and stable states, applied polarization voltage ΔV is 10 mV, respectively. Tafel curve of Li||Li symmetrical cells were tested from −1.5 V to 1.5 V with a scan rate of 1 mV/s using CHI660D electrochemical workstation. Electrochemical impedance spectroscopy (EIS) of fully charged state was carried out on Solartron Metrology at a frequency range of 10^5 Hz to 0.1 Hz.

2.4. Theoretical calculation

The DFT (density functional theory) calculation in this work was performed using the B3LYP-D3 method [26] and the 6–311 + G(d,p) basis set [27] within the Gaussian09 package [28]. The Gromacs 2018.8 software [29] was used to perform the MD (molecular dynamics) with OPLS-AA force field to describe the interactions. The relevant parameters were all obtained from the Sobtop program [30]. For the process, first, the packmol software [31] was used to build the simulated boxes. Next, energy minimization was performed on these boxes using the conjugate gradient method. Then, an equilibrium simulation was carried out in the NPT ensemble for 20 ns. Finally, a production simulation was conducted in the NVT ensemble for 5 ns. VMD software [32] was applied to visualize the electrolyte. The diffusion coefficient of Li can be determined by the following equation:

$$D = \frac{1}{6N_a}\lim_{t\to\infty}\frac{d}{dt}\sum_{i=1}^{Na}\langle[r_i(t)-r_i(0)]^2\rangle = \frac{1}{6}\lim_{t\to\infty}\frac{d}{dx}MSD$$

Where N_a means atoms' number $r_i(t)$ and $r_i(0)$ represent the position of atom i at time of t and 0, respectively. The mean-squared displacement (MSD) of Li$^+$ was obtained from MD results.

3. Results and discussion

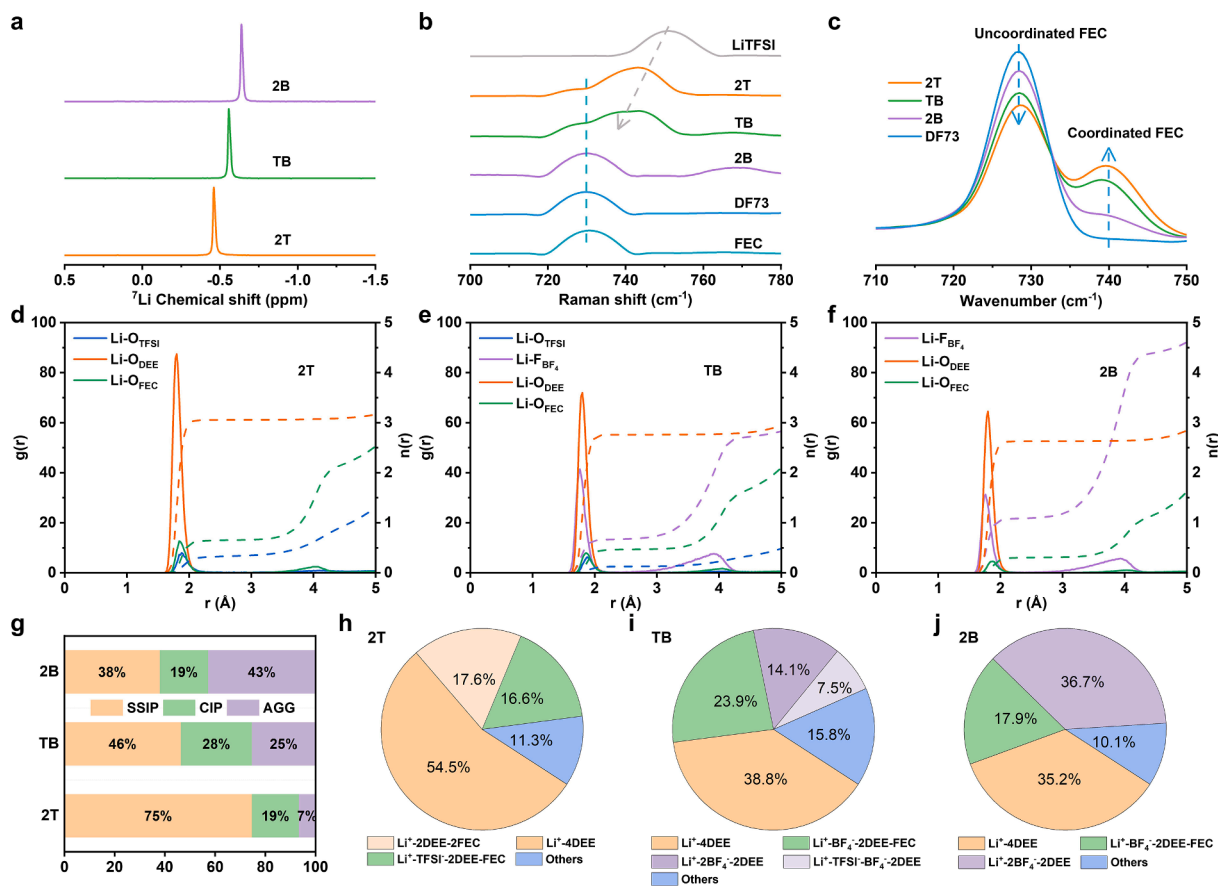The solvation structure is closely related to competitive coordination

Fig. 2. Characterization of the solvation structure in studied electrolytes. (a) ^{7}Li NMR spectra. (b) Raman spectra. (c) FT-IR spectra of C=O breathing vibration band for FEC. (d-f) Radical distribution functions (g(r), solid line) and coordination numbers (n(r), dashed line) of the Li-O (DEE, FEC, TFSI$^-$), Li-F (BF$_4^-$) pairs in different electrolytes. (g) Ratios of coordination structures. (h-j) Distributions of possible inner solvation shell compositions from MD simulations.

of anions and solvents with Li$^+$. Compared to the binding energy shown in **Fig. S2**, the BF$_4$ anion binds more tightly with Li$^+$, resulting in a higher electron cloud density around the Li$^+$. Consequently, the peak for 2B shifts to a higher field relative to 2 T in the ^{7}Li NMR spectra, with TB positioned between the two (Fig. 2**a**). The ^{19}F NMR spectra display peaks originating from three substances, as illustrated in **Fig. S3**. The chemical shift of ^{19}F nuclei in FEC follows the order: 2B **>** TB **>** 2T, indicating an increasing interaction between FEC and Li$^+$. For the ^{19}F nuclei in TFSI$^-$, the peak for TB is situated between 1 T and 2 T, while the ^{19}F chemical shift in BF$_4^-$ for TB is even more negative than that for 2B. The different trend can be attributed to the weaker dissociation of LiBF$_4$ compared to LiTFSI, leading to more accessible Li$^+$ for BF$_4^-$ when LiTFSI is added to 1B. Considering that the direct coordination sites of DEE, FEC and TFSI$^-$ with Li$^+$ are oxygen atoms, ^{17}O NMR tests were also conducted and the results were consistent with the above analysis (**Fig. S4**).

The Raman spectra also provide relevant coordination information as shown in Fig. 2**b**. The 750 cm^{-1} band is primarily ascribed to the S–N stretching in LiTFSI salt [33]. This band shifts to 742 cm^{-1} when the salt is dissolved in solvents for 2 T and TB, implying a decreased affinity between TFSI$^-$ and Li$^+$. For B–F symmetric vibration of BF$_4^-$ anion in the range of 750–800 cm^{-1}, although some studies have deconvolved this band into three peaks, the band observed in this study displays such weak intensity and inconspicuous changes that it is difficult to classify [34]. Thus, detailed coordination information about BF$_4^-$ is further disclosed by molecular dynamic (MD) simulation. The free FEC has three bands located at 731, 867, and 908 cm^{-1}, corresponding to the ring breathing mode, C–F stretching vibration, and ring skeleton deformation, respectively [35] (**Fig. S5**). These bands exhibit varying degrees of redshift in the mixture DF73, implying the miscibility interaction between DEE and FEC. No new peaks indicating FEC coordination with Li$^+$ are observed at 922 cm^{-1}, but the Fourier transform infrared reflection spectra (FT-IR) in Fig. 2**c** further elucidate its coordination state. A new peak at 740 cm^{-1} corresponding to the coordinated FEC, appears after the addition of salt. The increase in its intensity indicates that most FEC bonds with Li$^+$ in 2 T. This trend in intensity aligns with the above ^{19}F NMR analysis and can be attributed to the loose coordination between TFSI$^-$ and Li$^+$, which allows more solvents to approach Li$^+$.

Furthermore, MD simulations provide insights into the microscopic coordination structure of Li$^+$ in different electrolytes (Fig. 2**d–f**). According to the radical distribution functions (g(r)), a sharp peak corresponding to Li-O$_{DEE}$ pairs and a weaker peak corresponding to Li-O$_{FEC}$ pairs are observed at approximately 1.85 Å in all three electrolytes, supporting the notion that DEE solvents tend to be located within the inner sheath. Regarding the anions, only a small number of TFSI$^-$ anions are found within the inner solvation sheath. In contrast, a more notable peak corresponding to Li-F$_{BF4}$ suggests a higher probability of BF$_4^-$ being present in the inner layer. Additionally, the solvation structures in electrolytes with other ratios were also illustrated in **Fig. S6–S7**, revealing that the coordination of Li-O$_{TFSI}$ remains consistently low. However, as the BF$_4^-$ content increases, the Li-F$_{BF4}$ coordination initially increases linearly and then approaches saturation, making the investigation of the intermediate ratio point TB particularly representative. In all three electrolytes, the coordination number of Li-O$_{DEE}$ is greater than 2.5 (**Fig. S8**). Solvated solvent molecules are less susceptible to oxidation compared to free solvent molecules, which enhances the oxidative stability of ether solvents that are typically considered to have poor oxidative stability.

The proportions of SSIP, CIP and AGG are determined by counting the number of anions around Li$^+$ within 2.5 Å (Fig. 2**g**), with the 2 T electrolyte showing a predominant proportion of SSIP. Owing to strong affinity with Li$^+$, BF$_4^-$ is less likely to be displaced from the inner layer by solvents, resulting in a high prevalence of CIP and AGG structure in TB and 2B, which resemble high-concentration electrolytes. Moreover, specific collected structures are presented in Fig. 2**h–j**, where over 50 % of Li$^+$ are surrounded by four DEE molecules in 2 T electrolyte and a greater number of anions are involved in coordination in both TB and 2B

electrolytes. Additionally, AGG in TB electrolyte is mainly composed of Li$^+$-2BF$_4$-2DEE and Li$^+$-TFSI$^-$-BF$_4$-2DEE configurations, with the latter enhancing the contribution of TFSI$^-$ to decomposition.

The LUMO and HOMO energy levels were calculated to provide an initial estimation of the redox stability of each component(Fig. 3**a**). After coordinating with Li$^+$, the LUMO of the pairs is lower than that of the individual components. Among the neutral components, DEE has the highest LUMO energy level, indicating superior reduction stability. Although the LUMO energy level of FEC is slightly lower, it is still considered as a useful cosolvent because of beneficial reduction decomposition products on electrodes. As depicted in **Fig. 3b** and **Fig. S9**, the CV results of the reduction process in the range of 0–2.5 V show peaks around 0.7–0.8 V, which may attribute to the decomposition of solvents. Distinctive peaks emerge from 1.7 to 1.4 V with the reduction potential following the order of TB **>** 2B **>** 2T, and the peak currents of 2 T being the lowest. Different reduction behaviors between TB and 2B can be attributed to the higher concentration of Li$^+$ surrounding each BF$_4^-$ in TB, as previously elucidated through the ^{19}F NMR spectra. Accordingly, the reduction potential increases because the LUMO energy level of a single anion will decrease upon coordination with Li$^+$. Based on the aforementioned analysis of the solvation structure, there is a high proportion of Li$^+$-anion pairs in TB and 2B electrolytes that can be preferentially reduced, contributing to the anion-derived SEI. However, the extended decomposition plateau of 2B observed in the chronopotentiometry test suggests the possibility of excessive decomposition, which may result in a thicker interphase (**Fig. S10**). **Fig. S11** provides a comparison of the oxidation stability of electrolytes. The oxidation currents of TB and 2B significantly decreased in subsequent cycles, indicating that the initially formed SEI could effectively prevent the subsequent oxidation decomposition of electrolytes. In contrast, continuous high current of 2 T implied continuous consumption of the electrolyte, which is unfavorable for stable cycling.

To understand the interfacial kinetics of LMA, exchange current densities (j_0) of Li electrode can serve as an indicator [36]. As depicted in **Fig. 3c**, j0 in TB (0.402 mA cm^{-2}) is close to that of 2B (0.412 mA cm^{-2}), whereas it is somewhat lower in 2 T (0.277 mA cm^{-2}). Furthermore, the CV curves for Li plating/stripping in three electrolytes exhibit a consistent trend that 2 T shows the lowest current around nucleation potential and the smallest plating peak area, indicating an impeded transport kinetics (Fig. 3**d**). The activation energies of the charge-transfer process obtained by fitting the temperature-dependent electrochemical impedance spectroscopy (EIS) results also support this view (Fig. 3**e and** S12). A higher $E_{a,ct}$ indicates a slower process for Li$^+$ to get rid of solvents and a reduced flux of bare Li$^+$ around the LMA, which causes insufficient Li$^+$ to preferentially gather at the tips of nucleation sites, leading to dendritic Li deposition in 2 T. Conversely, the fast charge-transfer process in TB and 2B ensures a plentiful supply of Li$^+$ that acquire electrons at each Li nucleation site, facilitating the formation of close-packed Li deposits.

The efficiency of Li plating/stripping is evaluated by the Aurbach methods 3 using Li||Cu cells, in which TB and 2B show higher average Coulombic Efficiency (CE) than 2 T (Fig. 4**a**). Comparable CE in the three electrolytes can be attributed to the consistent solvent composition, as well as the generally good compatibility of ether-based solvents and FEC with lithium meal [37]. However, the morphology of deposited Li with the capacity of 5 mAh cm^{-2} on Cu substrate show significant differences (Fig. 4**b**). The Li deposits of 2 T are porous with seams, while a desired and smooth Li distribution is observed in TB and 2B. Fig. 4**a** only reflects a short-term Li plating/stripping process, so the stability of long-term cycling of LMA is further tested using Li||Li symmetric cells, as shown in Fig. 4**c**. The overpotentials are similar in the three electrolytes at the beginning and gradually increase over time. Throughout 1000 h, TB maintains a relatively low polarization voltage, whereas 2 T and 2B show a severalfold increase, exceeding 100 mV. Besides, a comparison of the EIS results for Li||Li cells after 50 cycles reveals that the cell with TB displays the lowest impedance (Fig. 4**d**). The Li||Li
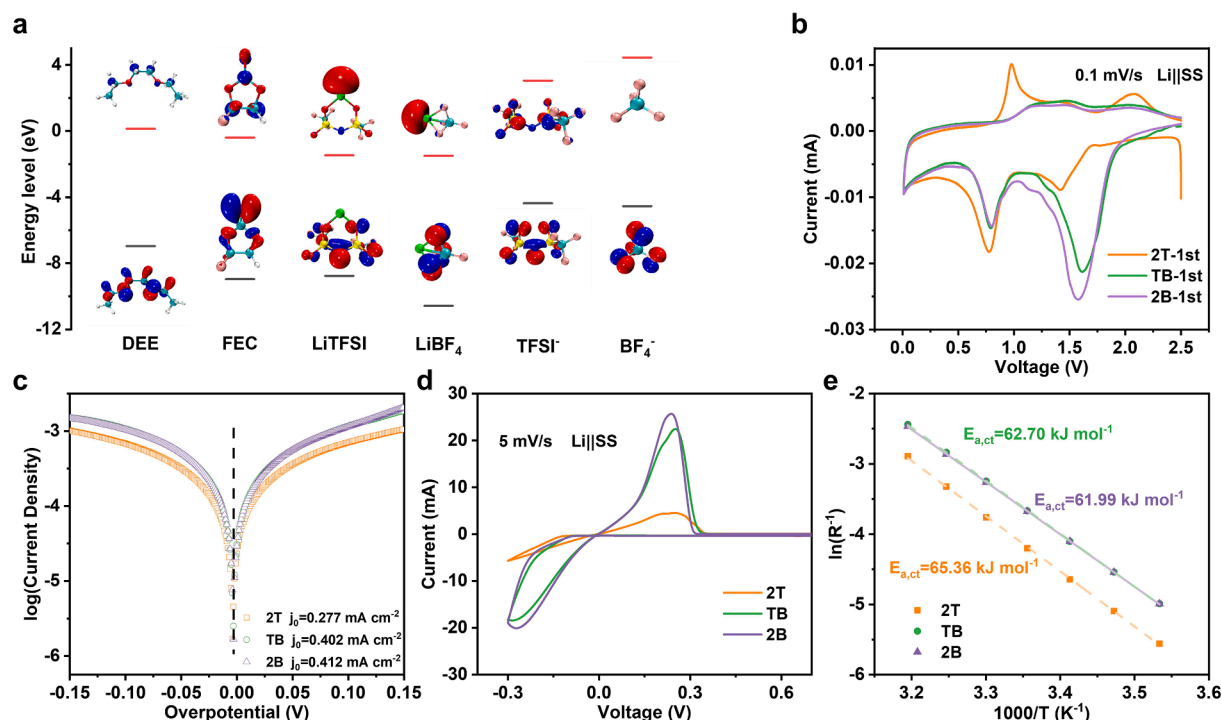
Fig. 3. (a) LUMO and HOMO energy levels of solvents, anions and Li$^+$-anion complex. (b) CV results of Li||SS between 0–2.5 V at 0.1 mV/s. (c) Tafel plots of Li||Li cells. (d) CV results of Li||SS scanned between − 0.3–0.6 V at 5 mV/s. (e) Arrhenius plot for the resistance of charge-transfer process.

symmetric cells with three electrolytes were further cycled at various temperatures, with 2 T exhibiting higher overpotentials across all temperatures (Fig. 4**e and** S13). Although the 2B electrolyte exhibits lower overpotentials at certain temperatures due to faster kinetics, its voltage curve becomes distorted and shows significant fluctuations at lower temperatures. High current rates accelerate interfacial degradation, as evidenced by a rapid increase in overpotential, with the effect being particularly pronounced for 2 T. (Fig. 4**f**). Moreover, durability tests under high-rate condition show fluctuating voltage profiles for 2B over 150 h, indicating the poor interface in 2B electrolyte (**Fig. S14**).

The Li||LCO or Li||NCM523 cells with three electrolytes are assembled and tested to evaluate the electrochemical stability. Fig. 5**a and** S15 compare the rate performance of the three electrolytes with two different thicknesses of Li foils. Under the condition with thin LMA, the impact of uneven Li deposition is more pronounced, leading to overall worsen performance and more noticeable difference among the electrolytes. Both TB and 2B deliver a high discharge capacity of 120 mAh g^{-1} even at 10C, while 2 T exhibits a significant drop in capacity at high rates. Besides, cells with TB and 2B display impressive stability, maintaining a capacity retention of 94.6 % and high CE of 99.8 % after 500 cycles as shown in Fig. 5**b**. However, the Li||LCO cells using 2 T shows rapid capacity degradation over 150 cycles, which can be attributed to poor compatibility with LMA and high impedance of the cathode electrolyte interphase (CEI) on the LCO cathodes (Fig. 5**c**). At the same time, the first semicircle representing the resistance of Li$^+$ migration through SEI for 2B is apparently larger than TB. This result can be attributed to increased decomposition of B-containing electrolytes components during film formation, coupled with the less ideal film-forming properties of LiBF$_4$ alone. This issue will be discussed in more detail later. Further studies under more stringent conditions, including high-loading cathodes and thin anodes, were conducted to assess the differences in cycling stability among the three electrolytes (Fig. 5**d**). TB owns the highest capacity retention of 88.7 % after 200 cycles, while 2 T shows a rapid decline in capacity similar to what is observed with low-loading cathodes. Cells assembled with NCM523 cathodes also exhibit similar trends in cycling and rate performance (Fig. 5**e and** S16). Corresponding

voltage profiles of NCM523 cathodes in Fig. 5**f** demonstrate less voltage hysteresis during discharge process with TB electrolyte.

The electrochemical performance of cells is closely related to the interfacial chemistry of electrodes. To investigate the effect of these three electrolytes on the electrode/electrolyte interface, Li||LCO cells were disassembled after 20 cycles. The resulting electrodes were then characterized using TEM and XPS to analyze their morphology and chemical composition. The XPS spectra of the cycled cathode are shown in Fig. 6**a**. The signals for C–C/C–H (284.8 eV in C 1 s) and C=O (288.4 eV in C 1 s and 531.6 eV in O 1 s, **Fig. S17**) primarily result from the oxidative decomposition of solvents, while the CF$_2$ and CF$_3$ signals mainly originate from the decomposition of FEC and LiTFSI [38]. In the 2 T electrolyte, stronger C–C/C–H and C=O signals were detected, indicating that solvents in the 2 T electrolyte is prone to decomposition. The CEI formed by the decomposition of a small amount of TFSI$^-$ is insufficient to suppress side reactions between the electrode and the electrolyte. As for the 2B electrolyte, solvent decomposition products are significantly reduced, and the resulting CEI is rich in inorganic components (B–F and LiF), primarily derived from the decomposition of LiBF$_4$. From the TEM images (Fig. 6**c**), it is evident that the CEI formed in 2B and 2 T is significantly thicker than that in TB, which hinders ion transport. Further comparison of the first-cycle in situ EIS of Li||LCO cells also shows that the cell with TB exhibits the lowest interfacial impedance, thereby enhancing the electrochemical performance of the battery (**Fig. S18**). In other words, the TB electrolyte forms an optimal solvation structure and a balanced organic–inorganic CEI, which effectively protects the electrode while ensuring a fast charge transfer process. Additionally, the CEI formed by the TB electrolyte contains both B-based (B–F, 194.5 eV in B 1 s and 686.1 eV in F 1 s) and N-based (Li$_3$N, 398.3 eV in N 1 s) components [39–41] (**Fig. S17**). The synergistic effect of these components helps suppress the degradation of the cathode and maintain the integrity of the particles (**Fig. S19**). The X-ray diffraction (XRD) pattern indicates that the (003) peak at 19.1° of cycled LCO cathode shifts to smaller angles, indicating the change in the c-axis (**Fig. S20**). The smallest shift observed in TB demonstrates the protective CEI, which can effectively enhance the electrochemical performance.
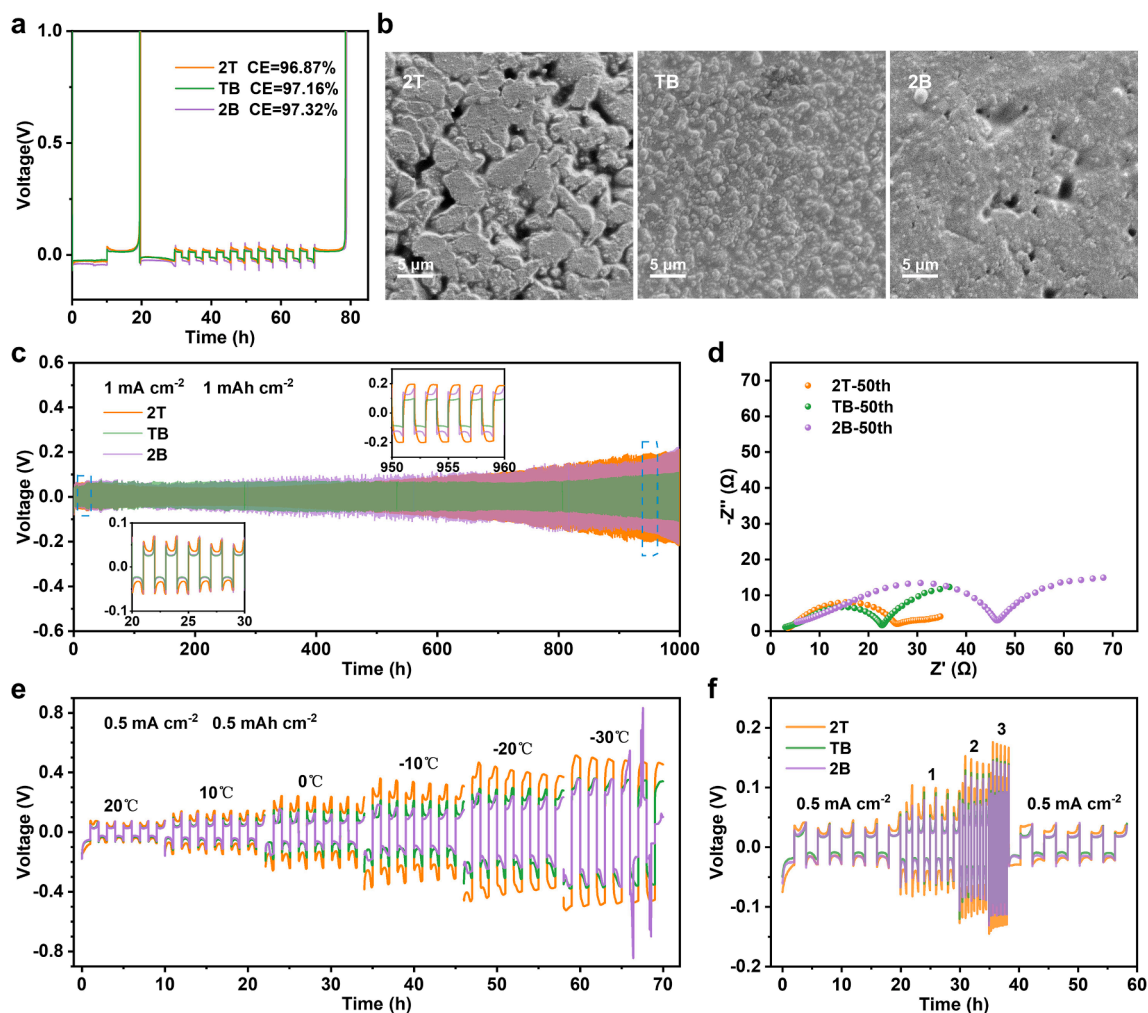
Fig. 4. (a) Coulombic Efficiency of Li metal by Aurbach protocol in Li||Cu half cells. (b) Surface morphologies of Li deposits on Cu foil. (c) Long cycling of Li||Li cells at 0.5 mA cm^{-2} and 1 mAh cm^{-2}, insets are enlarged charge–discharge curves. (d) EIS of the Li||Li cells after 50 cycles. (e) Voltage curves of Li||Li cells at different temperature at 0.5 mA cm^{-2} and 0.5 mAh cm^{-2}. (f) at room temperature and different rates.

XPS results of LMA also show similar components and trends to those of the cathode (Fig. 6b and S21). The distinct LiF signal indicates that a larger number of anions decompose at LMA in the 2B electrolyte. However, an excessive amount of inorganic components can lead to insufficient elasticity, making it less capable of accommodating the volume changes of LMA during cycling [42,43]. In the TB electrolyte, the increased and various inorganic species in the SEI enrich phase boundaries and vacancies, which is favorable for fast Li$^+$ diffusion. As shown in Fig. 6d, the surface of LMA cycled in 2 T is loose and porous, resulting in increased interfacial impedance and reduced capacity. Conversely, the morphology of LMA cycled in TB and 2B electrolytes is relatively dense and uniform, corresponding to their good cycling performance.

To explore the potential applications of electrolytes across a broad range of temperatures, the temperature-dependent properties of electrolytes were also tested. 2B shows the highest transference number, which is related to greater anions involvement in coordination (Fig. 7a and S22). However, this also results in a lower conductivity for 2B, possibly leading to increased polarization at room temperature (Fig. 7b). Moreover, 2B solidifies at −40 °C, while the other two remain in a liquid state (Fig. S23). With decreasing temperature, the difference in conductivity narrows as viscosity likely becomes the dominate factor. Given the consistent solvent composition of the electrolytes, the contact angle and viscosity are similar, although 2 T shows slightly higher values, likely due to the larger size and molecular weight of TFSI$^-$ anion (Fig. 7c

and S24). Based on the mean square displacement (MSD) plots as depicted in Fig. 7d, the fitted calculations reveal that the self-diffusion coefficient of TB is higher at both 25 °C and −20 °C. Improved ion transport within the bulk electrolyte contributes to a lower over-potential, with this effect being more pronounced at low temperatures. Fig. 7e shows the low-temperature discharge voltage curves of Li||LCO cells after charging at room temperature. It's apparent that the discharge plateau of 2 T at −30 °C changes to a slope profile due to increased polarization. When tested at −40 °C, the cells with 2B electrolyte cannot deliver discharge capacity because of the solidification of 2B, whereas cells with TB electrolyte provide a capacity as high as approximately 100 mAh/g. Furthermore, when the cells with TB electrolyte were cycled at −40 °C, the specific capacity increased initially due to the closer contact between the components, after which the cells could cycle stably for 50 cycles, exhibiting better applicability at various temperatures.

4. Conclusion

In summary, we reasonably screen two suitable lithium salts with distinct dissociation characteristics to investigate the impact of anion coordination on interfacial chemistry. Moreover, the dual-salt strategy involving the salts with significantly different binding abilities exhibits the advantages of low kinetic barrier for Li$^+$ desolvation and balanced film-forming properties. Compared with much less TFSI$^-$ inside the inner
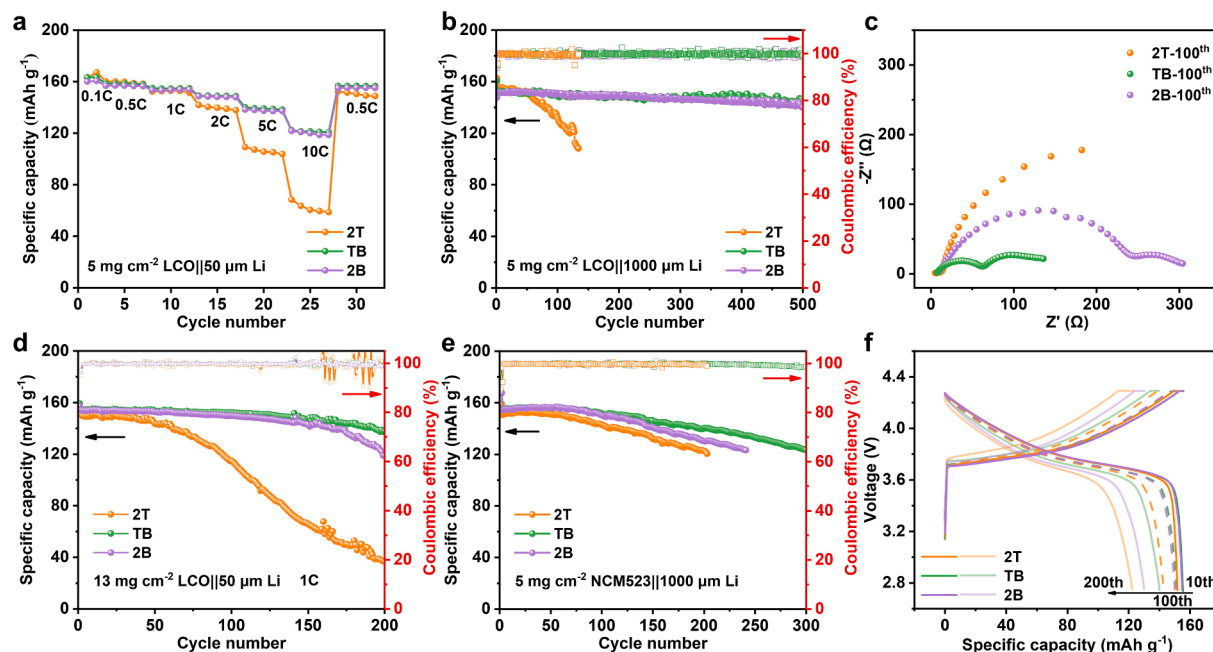
Fig. 5. (a) Rate capability ranging from 0.5 to 10C at 25 °C. (b, d, e) Cycling performance and Coulombic efficiency of LCO or NCM523 cathodes at 1C and 25 °C. (c) Nyquist spectra of LCO cathodes after 100 cycles. (f) Corresponding voltage profile of NCM523 cathode for 10th, 100th, 200th cycles.
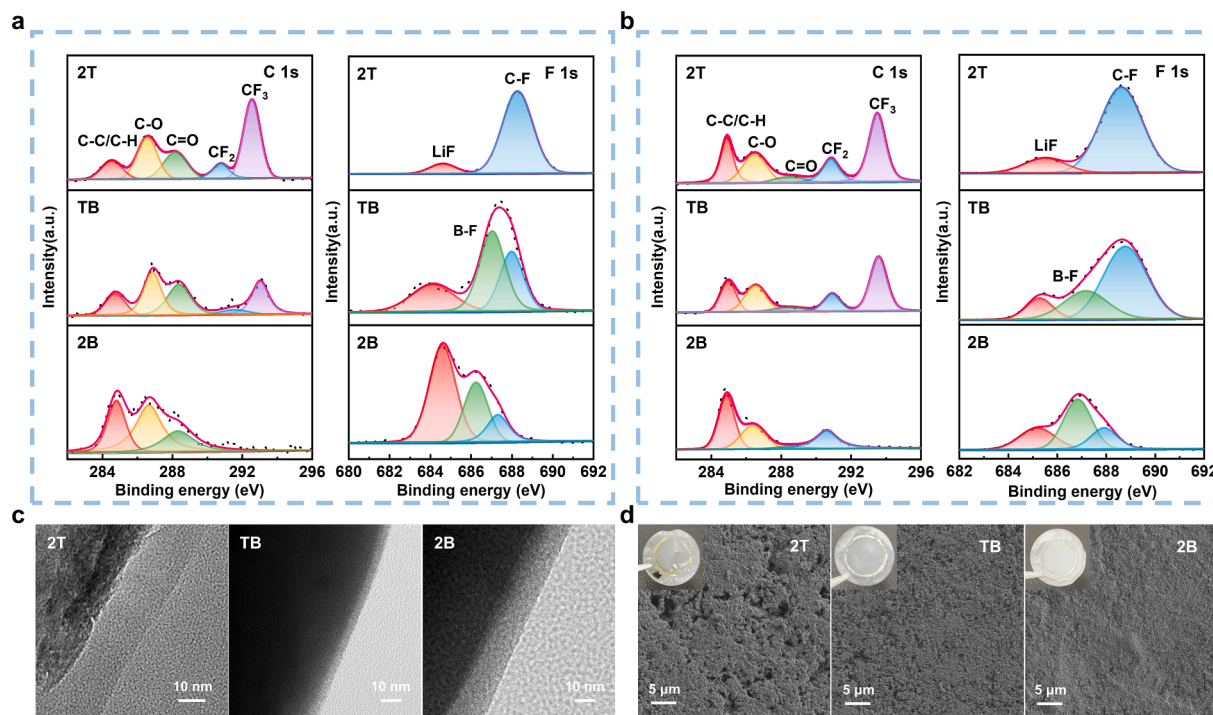

Fig. 6. XPS analysis of the SEI layer of electrodes after 20 cycles: C 1 s and F 1 s for (a) cathode and (b) LMA (c) TEM images of LCO cathodes after 20 cycles. (d) SEM images of LMA after 100 cycles, inset is the separator removed from the Li||LCO cells.

solvation sheath, the introduction of strongly associated LiBF$_4$ reduces the proportion of solvents entering the inner solvation sheath, promoting the formation of anion-derived SEI. However, excessive inorganic components in 2B lack sufficient elasticity to accommodate deformation during charge/discharge processes, leading to high interfacial impedance and impairing long-term cycling performance. In contrast, the dual-salt electrolyte not only exhibits moderate interfacial chemistry but also enables more facile Li$^+$ bulk transport. With these merits, the dual-salt electrolyte improves the compatibility with LMA, achieving a high

CE and low overpotential in Li||Li cells for over 1000 h. Moreover, this electrolyte demonstrates good long-term stability for LMBs at room temperature with 88.7 % capacity retention of full cells after 200 cycles, and shows feasibility at low temperature (cycled at −40 °C over 50 cycles). This work offers valuable insights for the dual-salt electrolyte to achieve effects similar to those of HCEs at just moderate concentrations, providing a straightforward approach to modify the solvation structure for advanced LMBs.
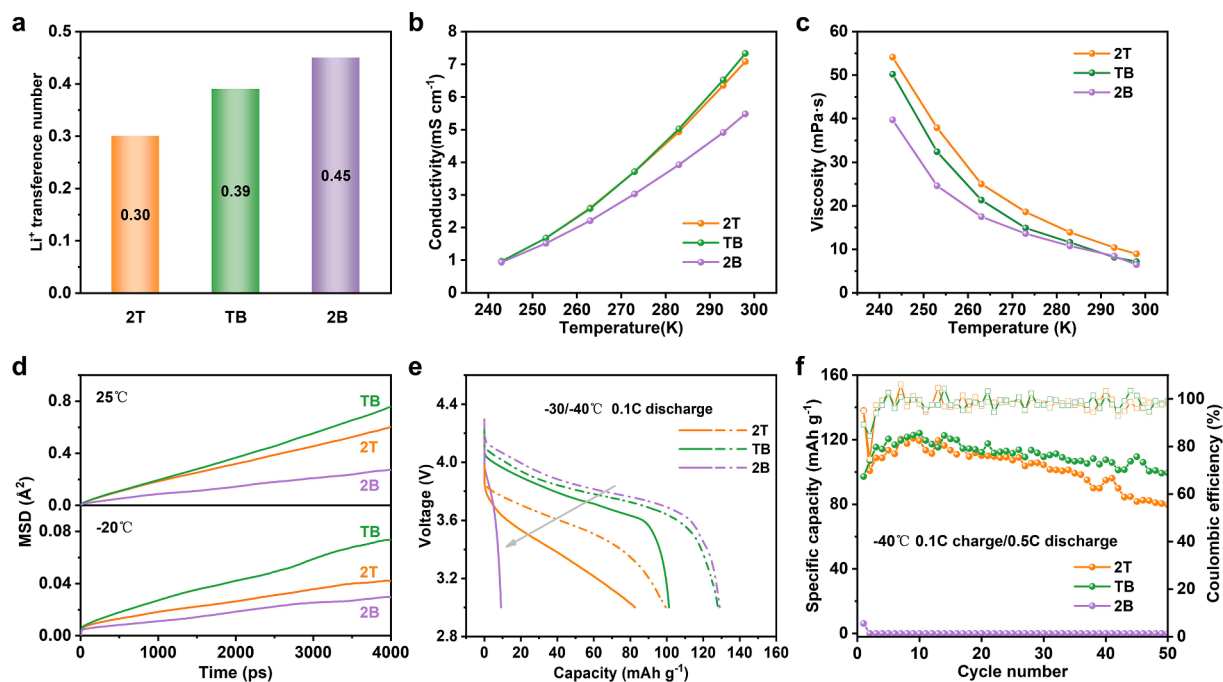
Fig. 7. (a) Li$^+$ transference number of the three electrolytes at 25 ℃. (b) The conductivity and (c) viscosity of three electrolytes at various temperatures. (d) Fitted MSD plots of the three electrolytes at 25 ℃ and −20 ℃. (e) The discharge curves of Li||LCO at −30/−40 ℃. (f) Cycling performance of Li||LCO cells at −40 ℃.

CRediT authorship contribution statement

Yaqi Zhang: Writing – original draft, Visualization, Validation, Investigation, Formal analysis, Data curation. **Pengbin Lai:** Writing – review & editing, Visualization, Validation, Methodology, Investigation, Formal analysis, Data curation. **Xiaodie Deng:** Writing – review & editing, Validation, Investigation. **Peng Zhang:** Writing – review & editing, Supervision, Methodology, Conceptualization. **Jinbao Zhao:** Writing – review & editing, Supervision, Project administration, Methodology, Conceptualization.

Declaration of competing interest

The authors declare that they have no known competing financial interests or personal relationships that could have appeared to influence the work reported in this paper.

Acknowledgement

Appendix A. Supplementary data

Supplementary data to this article can be found online at https://doi.org/10.1016/j.cej.2025.160482.

Data availability

Data will be made available on request.

References

[1] W. Xu, J. Wang, F. Ding, X. Chen, E. Nasybulin, Y. Zhang, J.-G. Zhang, Lithium metal anodes for rechargeable batteries, Energy Environ. Sci. 7 (2) (2014) 513–537, https://doi.org/10.1039/c3ee40795k.

[2] J. Liu, Z. Bao, Y. Cui, E.J. Dufek, J.B. Goodenough, P. Khalifah, Q. Li, B.Y. Liaw, P. Liu, A. Manthiram, Y.S. Meng, V.R. Subramanian, M.F. Toney, V. Viswanathan, M.S. Whittingham, J. Xiao, W. Xu, J. Yang, X.-Q. Yang, J.-G. Zhang, Pathways for practical high-energy long-cycling lithium metal batteries, *Nat Energy* 4 (3) (2019) 180–186, https://doi.org/10.1038/s41560-019-0338-x.

[3] P. Jing, M. Liu, H.-P. Ho, Y. Ma, W. Hua, H. Li, N. Guo, Y. Ding, W. Zhang, H. Chen, B. Zhao, J. Wang, M. Liu, Tailoring the Wadsley–Roth crystallographic shear structures for high-power lithium-ion batteries, Energy Environ. Sci. 17 (18) (2024) 6571–6581, https://doi.org/10.1039/d4ee02293a.

[4] J. Liu, P. Jing, L. Zheng, N. Guo, C. Liu, H. Wang, Diffusion tunnel shortening and Oxygen-Vacancy boosting high rate and stable lithium ion storage of crystallographic self-healed Ti2Nb10O29 anode, Chem. Eng. J. 482 (2024), https://doi.org/10.1016/j.cej.2024.148866.

[5] H. Wang, Z. Yu, X. Kong, S.C. Kim, D.T. Boyle, J. Qin, Z. Bao, Y. Cui, Liquid electrolyte: The nexus of practical lithium metal batteries, Joule 6 (2022) 1–29, https://doi.org/10.1016/j.joule.2021.12.018.

[6] S. Liu, C. Shu, Y. Yan, D. Du, T. Zeng, X. Wen, H. Xu, C. Zhao, X. Wang, G. Tian, Y. Zeng, Regulating solvation environment of Li ions via high donor number anions for high-performance Li-metal batteries, Chem. Eng. J. 450 (2022), https://doi.org/10.1016/j.cej.2022.138369.

[7] Y.-G. Cho, Y.-S. Kim, D.-G. Sung, M.-S. Seo, H.-K. Song, Nitrile-assistant eutectic electrolytes for cryogenic operation of lithium ion batteries at fast charges and discharges, Energy Environ. Sci. 7 (5) (2014) 1737–1743, https://doi.org/10.1039/c3ee43029d.

[8] Y. Yamada, J. Wang, S. Ko, E. Watanabe, A. Yamada, Advances and issues in developing salt-concentrated battery electrolytes, *Nat Energy* 4 (4) (2019) 269–280, https://doi.org/10.1038/s41560-019-0336-z.

[9] L.A. Schkeryantz, J. Zheng, W.D. McCulloch, L. Qin, S. Zhang, C.E. Moore, Y. Wu, Designing Potassium Battery Salts through a Solvent-in-Anion Concept for Concentrated Electrolytes and Mimicking Solvation Structures, Chem. Mater. 32 (24) (2020) 10423–10434, https://doi.org/10.1021/acs.chemmater.0c02983.

[10] X. Ren, X. Zhang, Z. Shadike, L. Zou, H. Jia, X. Cao, M.H. Engelhard, B.E. Matthews, C. Wang, B.W. Arey, X.Q. Yang, J. Liu, J.G. Zhang, W. Xu, Designing Advanced In Situ Electrode/Electrolyte Interphases for Wide Temperature Operation of 4.5 V Li||LiCoO2 Batteries, Adv. Mater. 32(49) (2020) e2004898. doi: 10.1002/adma.202004898.

[11] T. Feng, G. Yang, S. Zhang, Z. Xu, H. Zhou, M. Wu, Low-temperature and high-voltage lithium-ion battery enabled by localized high-concentration carboxylate electrolytes, Chem. Eng. J. 433 (2022), https://doi.org/10.1016/j.cej.2021.134138.

[12] P. Jiang, J. Zhang, T. Zhan, K. Zhang, W. Jian, D. Ruan, Constructing a Robust Cathode Electrolyte Interface for Aqueous Hybrid Lithium-Ion Batteries Via Regulating the Solvent–Solute Interaction in a Locally Concentrated Electrolyte,

ACS Mater. Lett. 6 (4) (2024) 1216–1223, https://doi.org/10.1021/acsmaterialslett.3c01478.

[13] Y.X. Yao, X. Chen, C. Yan, X.Q. Zhang, W.L. Cai, J.Q. Huang, Q. Zhang, Regulating Interfacial Chemistry in Lithium-Ion Batteries by a Weakly Solvating Electrolyte, Angew. Chem. Int. Ed. 60 (8) (2020) 4090–4097, https://doi.org/10.1002/anie.202011482.

[14] H. Hu, J. Li, Q. Zhang, G. Ding, J. Liu, Y. Dong, K. Zhao, M. Yu, H. Wang, F. Cheng, Non-concentrated electrolyte with weak anion coordination enables low Li-ion desolvation energy for low-temperature lithium batteries, Chem. Eng. J. 457 (2023), https://doi.org/10.1016/j.cej.2023.141273.

[15] S. Liu, Y. Yan, R. Zheng, G. Tian, X. Wang, C. Shu, An Amphiphilic Molecule Induced Anion-Enrichment Interface for Next-Generation Lithium Metal Batteries, Small (2024), https://doi.org/10.1002/smll.202407855.

[16] S. Liu, X. Yu, Y. Yan, T. Zeng, X. Wang, G. Tian, C. Wang, S. Wang, Y. Zeng, C. Shu, Dendrite-free lithium deposition enabled by interfacial regulation via dipole-dipole interaction in anode-free lithium metal batteries, Energy Storage Mater. 62 (2023), https://doi.org/10.1016/j.ensm.2023.102959.

[17] J. Tan, J. Matz, P. Dong, J. Shen, M. Ye, A Growing Appreciation for the Role of LiF in the Solid Electrolyte Interphase, Adv. Energy Mater. 11 (16) (2021), https://doi.org/10.1002/aenm.202100046.

[18] H. Zeng, K. Yu, J. Li, M. Yuan, J. Wang, Q. Wang, A. Lai, Y. Jiang, X. Yan, G. Zhang, H. Xu, J. Wang, W. Huang, C. Wang, Y. Deng, S.S. Chi, Beyond LiF: Tailoring Li2O-Dominated Solid Electrolyte Interphase for Stable Lithium Metal Batteries, ACS Nano 18 (3) (2024) 1969–1981, https://doi.org/10.1021/acsnano.3c07038.

[19] C. Wang, T. Ouyang, X. Wang, S. Liu, G. Tian, F. Fan, P. Liu, S. Wang, C. Zeng, C. Shu, Accelerating lithium ion transport via increasing the entropy of the electrolyte for stable lithium metal batteries, Journal of Energy, Chemistry 99 (2024) 384–392, https://doi.org/10.1016/j.jechem.2024.07.066.

[20] Z. Wen, W. Fang, F. Wang, H. Kang, S. Zhao, S. Guo, G. Chen, Dual-Salt Electrolyte Additive Enables High Moisture Tolerance and Favorable Electric Double Layer for Lithium Metal Battery, Angew. Chem. Int. Ed. 63 (13) (2024), https://doi.org/10.1002/anie.202314876.

[21] Y. Chen, Z. Yu, P. Rudnicki, H. Gong, Z. Huang, S.C. Kim, J.-C. Lai, X. Kong, J. Qin, Y. Cui, Z. Bao, Steric Effect Tuned Ion Solvation Enabling Stable Cycling of High-Voltage Lithium Metal Battery, J. Am. Chem. Soc. 143 (44) (2021) 18703–18713, https://doi.org/10.1021/jacs.1c09006.

[22] L. Cheng, Y. Wang, J. Yang, M. Tang, C. Zhang, Q. Zhu, S. Wang, Y. Li, P. Hu, H. Wang, An Ultrafast and Stable Li-Metal Battery Cycled at −40 °C, Adv. Funct. Mater. 33 (11) (2023) 2212349, https://doi.org/10.1002/adfm.202212349.

[23] Z. Xu, R. Huang, P. Huang, C. He, S. Liu, H. Zheng, W. Song, L. Shi, W. Gao, D. Li, H. Huang, H. Ying, W.-Q. Han, Weakly solvated electrolyte enables the robust solid electrolyte interface on SiOx anodes for lithium-ion battery, Chem. Eng. J. 500 (2024), https://doi.org/10.1016/j.cej.2024.157028.

[24] X. Wang, S. Li, W. Zhang, D. Wang, Z. Shen, J. Zheng, H.L. Zhuang, Y. He, Y. Lu, Dual-salt-additive electrolyte enables high-voltage lithium metal full batteries capable of fast-charging ability, Nano Energy 89 (2021) 106353, https://doi.org/10.1016/j.nanoen.2021.106353.

[25] B.D. Adams, J. Zheng, X. Ren, W. Xu, J.G. Zhang, Accurate Determination of Coulombic Efficiency for Lithium Metal Anodes and Lithium Metal Batteries, Adv. Energy Mater. 8 (7) (2017), https://doi.org/10.1002/aenm.201702097.

[26] A.D. Becke, Density-functional thermochemistry. III.The role of exact exchange, J. Chem. Phys. 98(7) (1993) 5648-5652. doi: 10.1063/1.3359469.

[27] T. Clark, C. Jayaraman, G.W. Spitznagel, P.V.R. Schleyer, Efficient Diffuse Function- Augmented Basis Sets for Anion Calculations. III.* The 3-21+G Basis Set for First-Row Elements, Li-F J. Comput. Chem. 4(3) (1982) 294-301. doi: 10.1002/jcc.540040303.

[28] M.J. Frisch, G.W. Trucks, D.J. Fox, Gaussian 09, Revision E. 01, Gaussian, Inc., Wallingford CT, (2013).

[29] M.J. Abraham, T. Murtola, R. Schulz, S. Páll, J.C. Smith, B. Hess, E. Lindahl, GROMACS: High performance molecular simulations through multi-level parallelism from laptops to supercomputers, SoftwareX 1–2 (2015) 19–25, https://doi.org/10.1016/j.softx.2015.06.001.

[30] T. Lu, Sobtop, Version 1.0(dev3.1),http://sobereva.com/soft/Sobtop (accessed on 2022-Aug-9).

[31] L. Martinez, R. Andrade, E.G. Birgin, J.M. Martinez, PACKMOL: a package for building initial configurations for molecular dynamics simulations, J. Comput. Chem. 30 (13) (2009) 2157–2164, https://doi.org/10.1002/jcc.21224.

[32] William Humphrey, Andrew Dalke, K. Schulten, VMD: Visual Molecular Dynamics, J. Mol. Graph. Model. 14(1) (1996) 33-38. doi: 10.1016/0263-7855(96)00018-5.

[33] D. Brouillette D.E. Irish N.J. Taylor G.r. Perron, M. Odziemkowski, J.E. Desnoyers, Stable solvates in solution of lithium bis(trifluoromethylsulfone)imide in glymes and other aprotic solvents: Phase diagrams, crystallography and Raman spectroscopyElectronic supplementary information (ESI) available: Crystallographic data (single crystal data) in cif format (CCDC reference number 184345). See Physical Chemistry Chemical Physics 4 24 2002 6063-6071 10.1039/b203776a http://www.rsc.org/suppdata/cp/b2/b203776a,.

[34] Z. Cao, M. Haruta, T. Doi, M. Inaba, Dilution Effects of Highly Concentrated LiBF4/DMC with Fluorinated Esters on Charge/Dishcharge Properties of Ni-rich LiNi0.8Co0.1Mn0.1O2 Positive Electrode, J. Electrochem. Soc. 167 (4) (2020), https://doi.org/10.1149/1945-7111/ab7181.

[35] G. Park, K. Lee, D.-J. Yoo, J.W. Choi, Strategy for Stable Interface in Lithium Metal Batteries: Free Solvent Derived vs Anion Derived, ACS Energy Lett. 7 (12) (2022) 4274–4281, https://doi.org/10.1021/acsenergylett.2c02399.

[36] Z. Tu, S. Choudhury, M.J. Zachman, S. Wei, K. Zhang, L.F. Kourkoutis, L.A. Archer, Fast ion transport at solid–solid interfaces in hybrid battery anodes, *Nat Energy* 3 (4) (2018) 310–316, https://doi.org/10.1038/s41560-018-0096-1.

[37] A. Mohammadi, S. Djafer, S. Sayegh, A.J. Naylor, M. Bechelany, R. Younesi, L. Monconduit, L. Stievano, Assessing Coulombic Efficiency in Lithium Metal Anodes, Chem. Mater. 35 (6) (2023) 2381–2393, https://doi.org/10.1021/acs.chemmater.2c03518.

[38] Z. Peng, X. Cao, P. Gao, H. Jia, X. Ren, S. Roy, Z. Li, Y. Zhu, W. Xie, D. Liu, Q. Li, D. Wang, W. Xu, J.G. Zhang, High-Power Lithium Metal Batteries Enabled by High-Concentration Acetonitrile-Based Electrolytes with Vinylene Carbonate Additive, Adv. Funct. Mater. 30 (24) (2020), https://doi.org/10.1002/adfm.202001285.

[39] C. Jiang, Q. Jia, M. Tang, K. Fan, Y. Chen, M. Sun, S. Xu, Y. Wu, C. Zhang, J. Ma, C. Wang, W. Hu, Regulating the Solvation Sheath of Li Ions by Using Hydrogen Bonds for Highly Stable Lithium-Metal Anodes, Angew. Chem. Int. Ed. Engl. 60 (19) (2021) 10871–10879, https://doi.org/10.1002/anie.202101976.

[40] J. Qiu, J. Guo, J. Li, Y. Wu, Z. Fan, H. Ye, Z. Fang, Z. Zhang, R. Zeng, Insight into the Contribution of the Electrolyte Additive LiBF(4) in High-Voltage LiCoO(2) SiO/C Pouch Cells, ACS Appl Mater Interfaces (2023), https://doi.org/10.1021/acsami.3c10903.

[41] C. Wang, S. Liu, H. Xu, X. Wang, G. Tian, F. Fan, P. Liu, S. Wang, C. Zeng, C. Shu, Adjusting Li+ Solvation Structures via Dipole–Dipole Interaction to Construct Inorganic-Rich Interphase for High-Performance Li Metal Batteries, Small 20 (24) (2024), https://doi.org/10.1002/smll.202308995.

[42] H. Shin, J. Park, S. Han, A.M. Sastry, W. Lu, Component-/structure-dependent elasticity of solid electrolyte interphase layer in Li-ion batteries: Experimental and computational studies, J. Power Sources 277 (2015) 169–179, https://doi.org/10.1016/j.jpowsour.2014.11.120.

[43] W. Zhang, Z. Shen, S. Li, L. Fan, X. Wang, F. Chen, X. Zang, T. Wu, F. Ma, Y. Lu, Engineering Wavy-Nanostructured Anode Interphases with Fast Ion Transfer Kinetics: Toward Practical Li-Metal Full Batteries, Adv. Funct. Mater. 30 (39) (2020), https://doi.org/10.1002/adfm.202003800.